nature medicine

Inhibition of TGF-β signaling in mesenchymal stem cells of subchondral bone attenuates osteoarthritis

Gehua Zhen[1,2], Chunyi Wen[3,4], Xiaofeng Jia[5], Yu Li[6], Janet L Crane[1,2], Simon C Mears[1], Frederic B Askin[7], Frank J Frassica[1], Weizhong Chang[1,2], Jie Yao[3], John A Carrino[1,8], Andrew Cosgarea[1], Dmitri Artemov[8], Qianming Chen[6], Zhihe Zhao[6], Xuedong Zhou[6], Lee Riley[1], Paul Sponseller[1], Mei Wan[1,2], William Weijia Lu[3,4] & Xu Cao[1,2]

Osteoarthritis is a highly prevalent and debilitating joint disorder. There is no effective medical therapy for the condition because of limited understanding of its pathogenesis. We show that transforming growth factor β1 (TGF-β1) is activated in subchondral bone in response to altered mechanical loading in an anterior cruciate ligament transection (ACLT) mouse model of osteoarthritis. TGF-β1 concentrations are also high in subchondral bone from humans with osteoarthritis. High concentrations of TGF-β1 induced formation of nestin-positive mesenchymal stem cell (MSC) clusters, leading to formation of marrow osteoid islets accompanied by high levels of angiogenesis. We found that transgenic expression of active TGF-β1 in osteoblastic cells induced osteoarthritis, whereas inhibition of TGF-β activity in subchondral bone attenuated the degeneration of articular cartilage. In particular, knockout of the TGF-β type II receptor (TβRII) in nestin-positive MSCs led to less development of osteoarthritis relative to wild-type mice after ACLT. Thus, high concentrations of active TGF-β1 in subchondral bone seem to initiate the pathological changes of osteoarthritis, and inhibition of this process could be a potential therapeutic approach to treating this disease.

Osteoarthritis is the most common degenerative joint disorder, afflicting mainly the weight-bearing joints, such as hips and knees, is the leading cause of physical disability and has been predicted to affect 67 million people in the United States by 2030 (ref. 1). Despite identified risk factors (for example, mechanical, metabolic or genetic factors) the exact pathogenesis of osteoarthritis remains unclear[2]. Currently there is no effective disease-modifying treatment for osteoarthritis, necessitating joint replacement as a therapeutic option[3,4].

Articular cartilage degeneration is the primary concern in osteoarthritis, which has recently been attributed to hypoxia-inducible factor-2α (HIF-2α)[5,6] and complement component 5 (C5)[7], in addition to the well-established factors ADAM metallopeptidase with thrombospondin type 1 motif, 5 (ADAMTS5)[8] and matrix metalloproteinase 13 (MMP13)[9]. The homeostasis and integrity of articular cartilage rely on its biochemical and biomechanical interplay with subchondral bone and other joint tissues[10]. Subchondral bone provides the mechanical support for overlying articular cartilage during the movement of load-bearing joints and undergoes constant adaptation in response to changes in the mechanical environment through modeling or remodeling[11]. As a result of instability of mechanical loading on such joints, for example, as occurs with ligament injury, excessive body weight or weakening muscles during aging, the subchondral bone and calcified cartilage zone undergo changes[12]. For instance, rupture of the ACL increases the risk of knee osteoarthritis[13], and approximately 20–35% of individuals with osteoarthritis are estimated to have had an incidental ACL tear[14,15]. Clinically, osteophyte formation, subchondral bone sclerosis, disruption of the tidemark accompanied by angiogenesis at the osteochondral junction and articular cartilage degeneration are characteristics of osteoarthritis[16]. Further, bone marrow lesions are closely associated with pain and have been implicated to predict the severity of cartilage damage in osteoarthritis[17]. In healthy articular cartilage, matrix turnover remains at relatively low rates, and chondrocytes resist proliferation and terminal differentiation[18]. During the progression of osteoarthritis, type X collagen, alkaline phosphatase, runt-related transcription factor 2 (RUNX2) and MMP13 are expressed in articular chondrocytes with low amounts of proteoglycans and expanded calcified cartilage zones in articular cartilage[2,19]. However, the exact mechanism underlying the potential contributions of defective subchondral bone to articular cartilage degeneration during osteoarthritis progression is largely unknown.

The role of TGF-β in the pathogenesis of osteoarthritis has drawn increasing attention in recent years. TGF-β is essential for the

[1]Department of Orthopaedic Surgery, School of Medicine, Johns Hopkins University, Baltimore, Maryland, USA. [2]Institute of Cell Engineering, School of Medicine, Johns Hopkins University, Baltimore, Maryland, USA. [3]Department of Orthopaedics and Traumatology, Li Ka Shing Faculty of Medicine, The University of Hong Kong, Pokfulam, China. [4]Center for Human Tissues and Organs Degeneration, Shenzhen Institute of Advanced Technology, Chinese Academy of Science, Shenzhen, China. [5]Department of Biomedical Engineering, School of Medicine, Johns Hopkins University, Baltimore, Maryland, USA. [6]State Key Laboratory of Oral Diseases, West China Hospital of Stomatology, Sichuan University, Chengdu, Sichuan, China. [7]Department of Pathology, School of Medicine, Johns Hopkins University, Baltimore, Maryland, USA. [8]Department of Radiology and Radiological Science, School of Medicine, Johns Hopkins University, Baltimore, Maryland, USA. Correspondence should be addressed to X.C. (xcao11@jhmi.edu).

Received 12 December 2012; accepted 21 February 2013; published online 19 May 2013; doi:10.1038/nm.3143

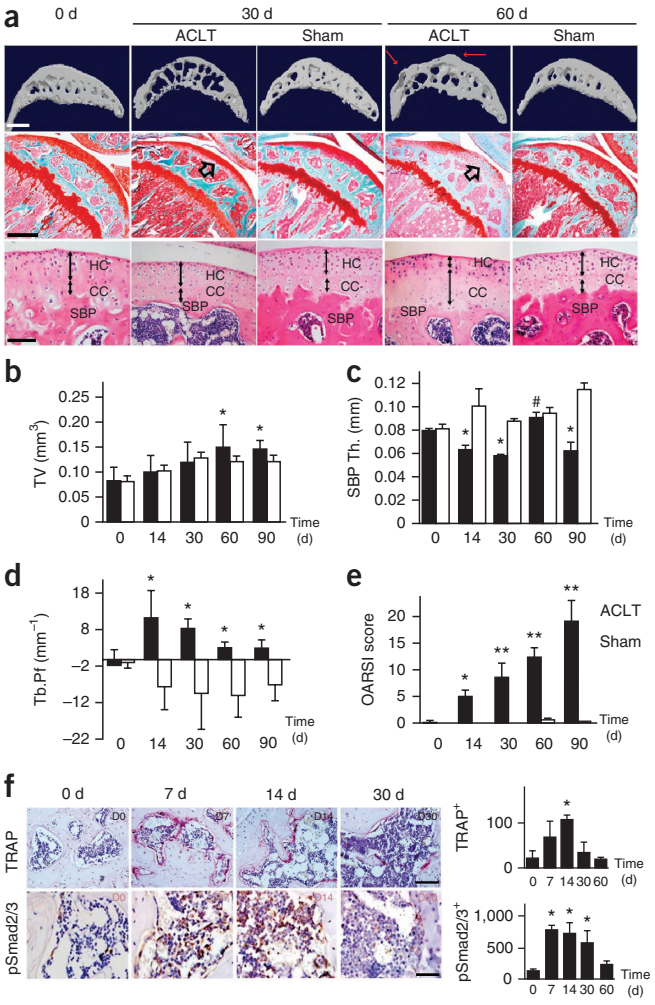

Figure 1 Upregulated TGF-β signaling in the subchondral bone is associated with changes of subchondral bone architecture in ACLT mice. (**a**) Top, three-dimensional high-resolution μCT images of the tibial subchondral bone medial compartment (sagittal view) at 0, 30 and 60 d after sham operation or ACLT surgery. Red arrows indicate altered morphology of the SBP. Scale bar, 500 μm. Middle, safranin O and fast green staining of sagittal sections of the tibia medial compartment, proteoglycan (red) and bone (blue). Black open arrows indicate loss of proteoglycan at 30 and 60 d after surgery. Scale bar, 500 μm. Bottom, H&E staining of the SBP and cartilage. The hyaline cartilage (HC) and calcified cartilage (CC) thicknesses are indicated by double-headed arrows. Scale bars, 100 μm. (**b**–**d**) Quantitative analysis of total tissue volume (TV; **b**), thickness of SBPs (SBP Th.; **c**) and Tb.Pf (**d**) in subchondral bone determined by μCT analysis. $n = 8$ per group. $^{*}P < 0.05$ compared to the sham-operated group at the corresponding time points; $^{\#}P < 0.05$ compared to the ACLT group at 30 d after surgery. (**e**) OARSI scores at 0–90 d after surgery. $n = 8$ per group. $^{*}P < 0.05$, $^{**}P < 0.01$ compared to the sham-operated group at the corresponding time points. (**f**) TRAP staining (magenta, top) and immunohistochemical analysis of pSmad2/3^{+} cells (brown, bottom) in mouse tibial subchondral bone after ACLT surgery. Scale bars, 200 μm (top); 100 μm (bottom). On the right is a quantitative analysis of the number of TRAP^{+} and pSmad2/3^{+} cells per bone marrow area (mm^{2}). $n = 8$ per group. $^{*}P < 0.05$ compared to the day 0 group. All statistical significance was determined by multifactorial analysis of variance (ANOVA), and all data are shown as the mean ± s.d.

maintenance of articular cartilage metabolic homeostasis and structural integrity[20]. It also stimulates chondrocyte proliferation, and knockout of TGF-β1 or interruption of TGF-β signaling in articular cartilage results in loss of proteoglycans and cartilage degeneration in mice[21,22]. The predominance of phosphorylated Smad1 and Smad5 (pSmad1/5) due to the elevated expression ratio of ALK1 to ALK5 in articular cartilage might contribute to the pathogenesis of osteoarthritis[23–25]. Several groups have demonstrated that ablation of endogenous TGF-β1 activity suppresses osteophyte formation *in vivo* but aggravates articular cartilage degeneration in osteoarthritis mice models[26,27]. We have previously shown that TGF-β1 is activated during osteoclastic bone resorption and induces the migration of bone marrow MSCs to resorption pits for new trabecular bone formation in the long bone, serving as a coupling factor[28]. In this study we investigated the role of TGF-β1 in subchondral bone pathology and articular cartilage degeneration during the progression of osteoarthritis. We found that inhibition of TGF-β1 activity in subchondral bone attenuated its pathological changes and led to less degeneration of articular cartilage relative to untreated groups in different osteoarthritis rodent models.

RESULTS

Elevated TGF-β levels in subchondral bone after ACLT

To examine subchondral bone changes at the onset of osteoarthritis, we transected the ACL in 2-month-old mice to generate a destabilized osteoarthritis animal model and analyzed the effects over time. The tibial subchondral bone volume in ACLT mice changed substantially relative to sham-operated control mice after surgery as determined by three-dimensional microcomputed tomography (μCT) analysis (**Fig. 1a**). The total subchondral bone tissue volume was more than 20% higher in the ACLT mice compared to sham-operated controls by 2 months after surgery (**Fig. 1b**). The thickness of the subchondral bone plate (SBP) fluctuated significantly in the ACLT mice from 14 to 60 d after surgery, with abnormal morphology present by 60 d (**Fig. 1c**). Moreover, the disruption of the connectivity and microarchitecture of trabecular bone was indicated by a significantly higher trabecular pattern factor (Tb.Pf)[29] in the ACLT mice compared to sham-operated controls (**Fig. 1d**), indicating uncoupled bone remodeling. We also observed the pathological changes in subchondral bone in the knee joints of humans with osteoarthritis (**Supplementary Fig. 1**).

We observed proteoglycan loss in cartilage in the ACLT mice at 30 d after surgery, which was further aggravated at 60 d (**Fig. 1a**). Notably, we detected proteoglycan loss at the deep zone of articular cartilage in the ACLT mice. H&E staining showed that the thickness of the calcified cartilage zone in these mice was greater than that in age-matched sham-operated mice, with the tidemark moving closer to the articular surface. (**Fig. 1a**). Osteoarthritis Research Society International (OARSI) scores[30] revealed degeneration of articular cartilage that started at 14 d after ACLT and progressed gradually (**Fig. 1e**). Indeed, in a computerized simulation model for human knee joints, expansion and increased stiffness of subchondral bone changed the distribution of articular cartilage stress (**Supplementary Fig. 2**).

TRAP staining showed that the number of osteoclasts increased in subchondral bone as early as 7 d after ACLT, and the continued osteoclastic bone resorption generated large bone marrow cavities by 30 d (**Fig. 1a,f**). Immunostaining demonstrated that after surgery, the number of cells positive for phosphorylated Smad2/3 (pSmad2/3^{+}) was higher at 7 d as compared to baseline at day 0, remained at high concentrations until 30 d and then returned to approximate baseline numbers by 60 d (**Fig. 1f**). These results suggest that altered mechanical loading induced subchondral bone resorption with elevated active TGF-β concentrations in this region.

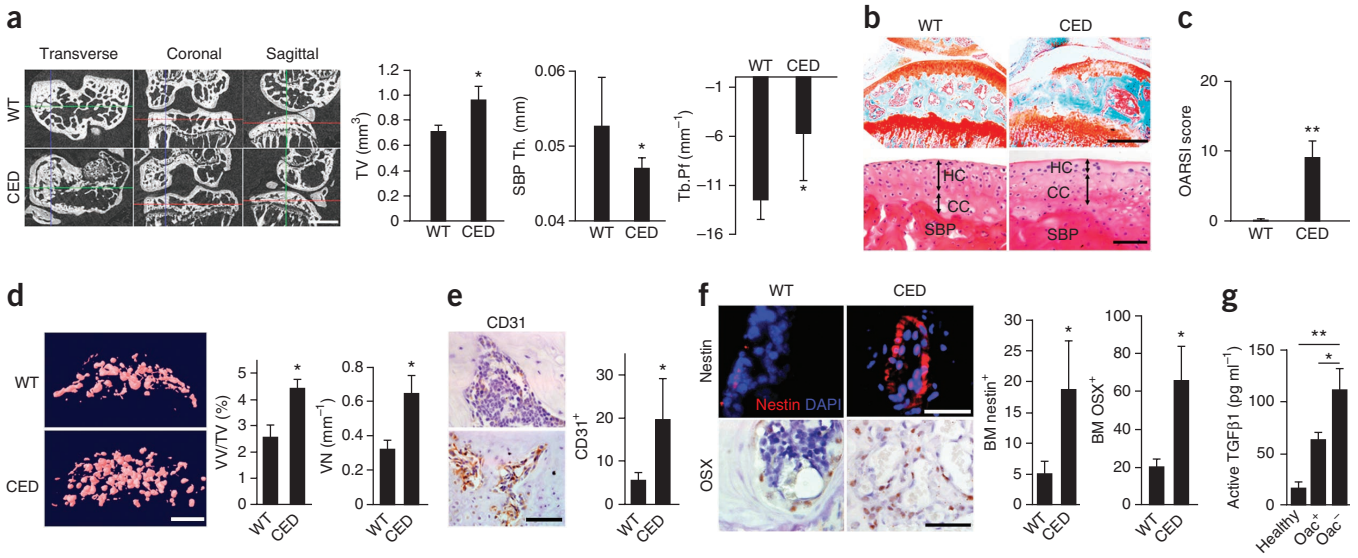

Figure 2 CED mice with transgenic activating mutation of TGF-β1 show a knee osteoarthritis phenotype. (**a**) Representative μCT images of transverse, coronal and sagittal views of the tibia subchondral bone of 4-month-old CED mice and WT littermates. Scale bar, 1mm. On the right is a quantitative analysis of structural parameters of subchondral bone. (**b**) Safranin O and fast green (top) and H&E (bottom) staining of sagittal sections of the tibia medial compartment. Scale bars, 500 μm (top); 100 μm (bottom). Double-headed arrows indicate the hyaline cartilage and calcified cartilage thicknesses. (**c**) OARSI scores of CED mice and WT littermates. (**d**) CT-based microangiography of the tibia subchondral bone of CED mice and WT littermates, with a quantification of vessel volume relative to tissue volume (VV/TV) and vessel number (VN) shown on the right. Scale bar, 500 μm. (**e**,**f**) Immunohistochemical (**e**) and immunofluorescent (**f**) analyses of CD31$^+$ (brown; **e**), nestin-positive (red; **f**, top and osterix (OSX)-positive (brown; **f**, bottom) cells. Scale bars, 50 μm (**e**); 50 μm (**f**, top); 100 μm (**f**, bottom). In the top row of **f**, blue indicates DAPI staining of nuclei in the tibial subchondral bone of CED mice and WT littermates. Also shown in **f** are quantifications of the number of bone marrow (BM) cells positive for nestin and osterix (per mm^2). (**g**) ELISA analysis of active TGF-β1 in conditioned medium of a human tibia subchondral bone specimen. Healthy, subchondral bone collected from healthy donors; Oac$^+$, subchondral bone with articular cartilage from an individual with osteoarthritis; Oac$^-$, subchondral bone without articular cartilage from an individual with osteoarthritis. $n = 10$ per group (**a**–**g**). $^*P < 0.05$, $^{**}P < 0.01$ determined by multifactorial ANOVA. All data are reported as the mean ± s.d.

Expression of active TGF-β1 in bone induces osteoarthritis

In Camurati-Engelmann disease (CED), TGF-β1 is activated after secretion as a result of a point activating mutation in the Tgfb1 gene[28,31], and people with CED are prone to developing osteoarthritis[20,32]. To examine whether high concentrations of active TGF-β1 in subchondral bone initiate osteoarthritis, we used a CED activation mutation mouse model in which TGF-β1 is activated after secretion in the subchondral bone marrow by osteoblastic cells. Three-dimensional μCT images of cross-sectional, coronal and sagittal views of tibial subchondral bone showed an uneven distribution of bone mass in CED mice relative to wild-type (WT) littermates, indicating disrupted bone formation (**Fig. 2a**). Similarly to in the ACLT mouse model, the tibial subchondral bone tissue volume and Tb.Pf were greater, whereas the thickness of the SBP was less, in CED mice relative to their WT littermates. Notably, we detected markedly lower proteoglycan expression at the calcified cartilage zone adjacent to the SBP in the CED mice (**Fig. 2b**). Compared to WT littermates, the thickness of the calcified cartilage layer was greater in the CED mice, whereas the thickness of the hyaline cartilage layer was less and had apparent hypocellularity (**Fig. 2b**). OARSI scores revealed significant degeneration of articular cartilage in CED mice relative to age-matched WT littermates (**Fig. 2c**).

We also measured angiogenesis in these mice using microfil contrast–enhanced angiography, as elevated angiogenesis is a pathological manifestation of osteoarthritis[33]. The volume fraction and number of blood vessels in subchondral bone were significantly higher in CED mice relative to their WT littermates (**Fig. 2d**). Consistently, the number of CD31$^+$ endothelial progenitor cells was also higher (**Fig. 2e**). Immunostaining for nestin, which is expressed primarily in adult bone marrow MSCs[34,35], revealed a significantly higher number of nestin-positive cells in the subchondral bone marrow of CED mice compared to WT controls (**Fig. 2f**). Once committed to the osteoblast lineage, MSCs express osterix, a marker of osteoprogenitors. The number of osterix-positive osteoprogenitors was also significantly higher in the subchondral bone marrow of CED mice compared to WT controls (**Fig. 2f**), indicating that nestin-positive MSCs undergo osteoblastic differentiation to contribute to *de novo* bone formation. We also observed clustering of osterix-positive osteoprogenitors in the bone marrow cavity in the subchondral bone of ACLT mice (**Supplementary Fig. 3**).

In addition, we measured active TGF-β1 in subchondral bone of human knee joints at different stages of osteoarthritis. ELISA analysis showed that the concentrations of active TGF-β1 in the subchondral bone of knee joints of people with osteoarthritis were significantly higher than in those of healthy controls (**Fig. 2g**). Collectively, development of the knee joint osteoarthritis phenotype in CED mice was similar to that observed in the ACLT mouse model, revealing that high concentrations of active TGF-β1–induced abnormal subchondral bone formation may contribute to the degeneration of articular cartilage.

Inhibition of TGF-β signaling attenuates cartilage damage

We next examined the effects of inhibition of TGF-β activity on the joints of ACLT mice. Injection of a TβRI inhibitor (SB-505124) has been shown to rescue uncoupled bone formation induced by high concentrations of active TGF-β1 (ref. 28). We screened different

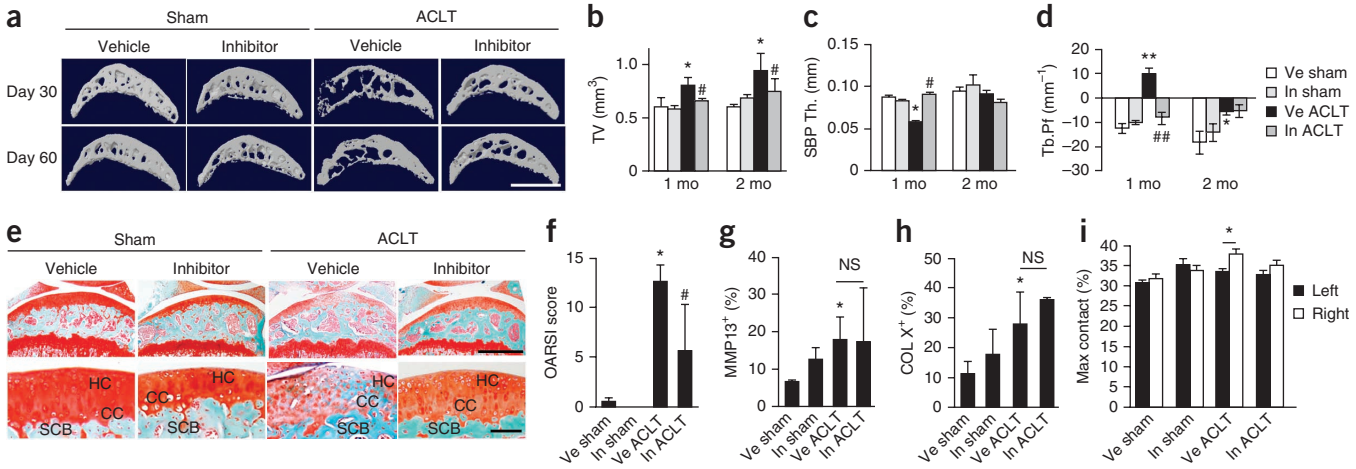

Figure 3 TβRI inhibitor stabilizes the subchondral bone microarchitecture and attenuates articular cartilage degeneration in ACLT mice. (**a**) Three-dimensional μCT images of the tibia subchondral bone medial compartment (sagittal view) of mice treated with 1 mg per kg body weight of the TβRI inhibitor daily for 30 d and analyzed 1 or 2 months after ACLT or sham surgery. Scale bar, 1 mm. (**b**–**d**) Quantitative analysis of structural parameters of subchondral bone by μCT analysis. Ve, vehicle; In, TβRI inhibitor. (**e**) Safranin O and fast green staining of articular cartilage in sagittal sections of the tibia medial compartment of mice treated with vehicle or inhibitor for 1 month and analyzed 2 months after ACLT or sham surgery. Scale bars, 500 μm (top); 100 μm (bottom). (**f**) OARSI scores of sham-operated and ACLT mice treated with either vehicle or TβRI inhibitor. (**g**,**h**) Quantitative analysis of the percentage of $MMP13^+$ and type X collagen (COL X)-positive chondrocytes in immunohistochemically stained articular cartilage tissue sections. (**i**) Percentages of maximum (Max) contact time in the gait analysis of mice at 2 months after ACLT or sham surgery treated with vehicle or inhibitor for 1 month. $n = 8$–12 per group. $^*P < 0.05$, $^{**}P < 0.01$ compared to the vehicle-treated sham-operated group; $^{\#}P < 0.05$, $^{\#\#}P < 0.01$ compared to the vehicle-treated ACLT group. NS, not significant. Statistical significance was determined by multifactorial ANOVA. All data are reported as the mean ± s.d.

doses of the TβRI inhibitor in ACLT mice to identify the optimal dose (**Supplementary Fig. 4**). Low concentrations of the TβRI inhibitor (0.1 or 0.5 mg per kg body weight) had minimal effects on subchondral bone, whereas higher concentrations, beginning at 1 mg per kg body weight, improved subchondral bone structure (**Fig. 3a**). Conversely, proteoglycan loss in articular cartilage was induced at higher concentrations (2.5 or 5 mg per kg body weight) (**Supplementary Fig. 4a**). Of note, we observed proteoglycan loss induced by higher doses of the inhibitor primarily in the superficial to middle zones of articular cartilage (**Supplementary Fig. 4a**). As treatment with the TβRI inhibitor prevented uncoupled bone resorption and formation (**Supplementary Fig. 5**), we found improvement of trabeculae connectivity and microarchitecture with 1 mg per kg body weight of the TβRI inhibitor, as demonstrated by normalization of subchondral bone tissue volume (**Fig. 3b**), maintenance of the thickness of the SBP (**Fig. 3c**) and a lower volume in Tb.Pf relative to vehicle-treated ACLT mice (**Fig. 3d**). Notably, proteoglycan loss and calcification of articular cartilage were attenuated in ACLT mice 2 months after surgery, a time point that is often used for analysis in destabilized osteoarthritis mice models[36] (**Fig. 3e**). We quantified the protective effect of the TβRI inhibitor on articular cartilage in TβRI inhibitor–treated compared to vehicle-treated ACLT mice using the OARSI system (**Fig. 3f**). The inhibitor, however, had no significant effects on the elevated concentrations of MMP13 or type X collagen in chondrocytes as compared to vehicle treatment (**Fig. 3g**,**h**).

We repeated the TβRI inhibitor treatment experiments in 9-month-old mice with ACLT or sham operation. Similarly, subchondral bone structure was improved and articular cartilage degeneration was attenuated in ACLT mice treated with 1 mg per kg body weight of the TβRI inhibitor (**Supplementary Fig. 6**). Moreover, gait analysis with the CatWalk system revealed significant disparity between the percentages of maximum contact time of the two hind limbs at 2 months after surgery, which was rescued in the inhibitor-treated ACLT group (**Fig. 3i**). Taken together, these results indicate that TGF-β has distinct roles in subchondral bone and articular cartilage, and inhibition of TGF-β activity in subchondral bone may prevent the degeneration of articular cartilage during osteoarthritis development.

Increase of MSCs leads to formation of osteoid islets

To examine the cellular mechanism of TβRI inhibitor–attenuated progression of osteoarthritis, we analyzed the effect of the TβRI inhibitor on MSCs in subchondral bone. We found by immunostaining that the number of nestin-positive MSCs in the subchondral bone marrow was substantially higher by 30 d after surgery in ACLT mice compared to sham-operated controls (**Fig. 4a**). This effect was prevented by the TβRI inhibitor (**Fig. 4a**). Similarly, osterix-positive osteoprogenitors were located largely on the bone surface in sham-operated controls (**Fig. 4a**), and the significantly higher number of osteoprogenitor clusters detected in the bone marrow of vehicle-treated ACLT mice was attenuated with TβRI inhibitor treatment (**Fig. 4a**). We confirmed these results using a flow cytometry analysis of nestin-positive MSCs and osterix-positive osteoprogenitors from subchondral bone (**Fig. 4**). We found osteocalcin-positive osteoblasts and osteoids as islets in the subchondral bone marrow of ACLT mice. As compared to vehicle-treated ACLT mice, injection of the TβRI inhibitor resulted in less abnormal localization, as the osteocalcin-positive osteoblasts and osteoid were located largely on the bone surface, which was similar to their location in the sham-operated controls (**Fig. 4b**). Formation of osteoid islets was lower in the TβRI inhibitor–treated group as compared to the vehicle-treated group in fluorescent double-labeling experiments (**Fig. 4d**).

Phosphorylation of Smad1 can be activated by TGF-β1 in endothelial progenitor cells[37]. Thus, we examined whether TGF-β1 activates phosphorylation of Smad1 in MSCs. We found that TGF-β1 stimulated

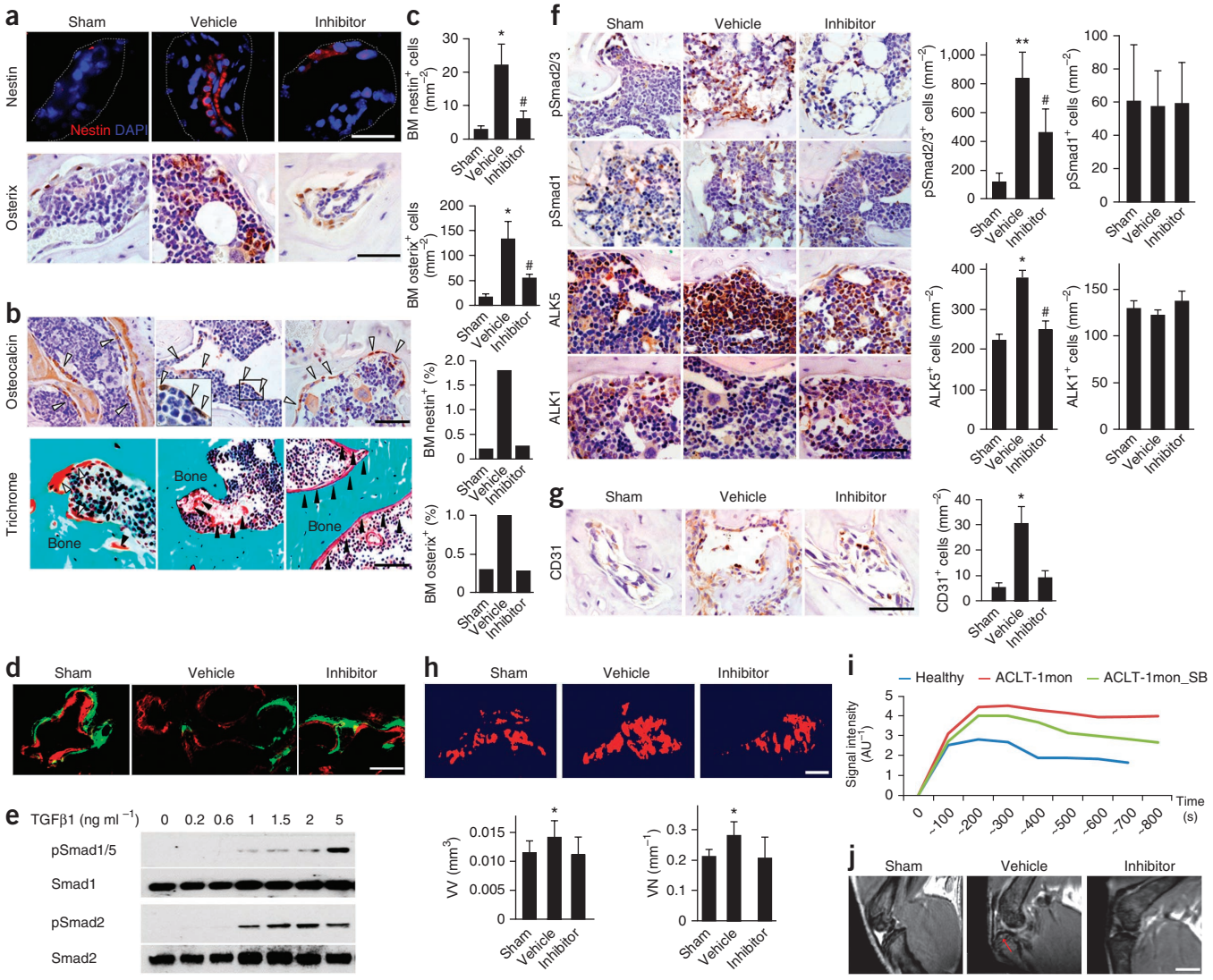

Figure 4 TβRI inhibitor reduces uncoupled bone formation and angiogenesis in ACLT mice. (**a**) Immunofluorescent and immunohistochemical analyses (left) and quantification (right) of nestin (red) and osterix (brown) in tibial subchondral bone collected 1 month after sham operation and treatment with vehicle (sham), ACLT operation and treatment with vehicle (vehicle) or ACLT operation and treatment with TβRI inhibitor (inhibitor). Blue in the top row indicates DAPI staining of nuclei. Scale bars, 50 μm. Outlines in the top row indicate the bone surface. (**b**) Immunohistochemical analysis of osteocalcin (brown) and trichrome staining in tibial subchondral bone sections. Scale bars, 50 μm. Open arrowheads indicate osteocalcin-positive cells, and closed arrowheads indicate osteoids. The magnification of the inset in the top center image is ×1,000. (**c**) Flow cytometry analysis of nestin and osterix in bone marrow from mouse subchondral bone. (**d**) Calcein (green) and xylenol orange (orange) fluorescent double labeling of the newly formed bone. Scale bar, 100 μm. (**e**) Western blot analysis of pSmad1/5, Smad1, pSmad2 and Smad2 in cultured MSCs treated with increasing doses of recombinant human TGF-β1. (**f**) Immunohistochemical analysis (left) and quantification of the number of pSmad2/3$^+$, pSmad1$^+$, ALK5$^+$ and ALK1$^+$ (all stained brown in the images on the left) cells (per mm^2) in the subchondral bone of mice 2 weeks after surgery. Scale bar, 50 μm. (**g**) Immunohistochemical analysis (left) and quantification of CD31$^+$ (brown in the images on the left) cells (per mm^2; right) in subchondral bone. Scale bar, 50 μm. (**h**) CT-based microangiography of the tibia subchondral bone (top) and quantification of subchondral bone vessel volume and vessel number (bottom). Scale bar, 500 μm. (**i**) Perfusion rate obtained by T1-weighted MRI scanning with contrast. AU, arbitrary units; ACLT-1mon; ACLT mice after treatment with vehicle for 1 month; ACLT-1mon_SB, ACLT mice after treatment with the TβRI inhibitor SB-505124 for 1 month. (**j**) Representative MRI T2-weighted images. The red arrow indicates a bone marrow lesion. $n = 8$–12 per group. $^*P < 0.05$, $^{**}P < 0.01$ compared to the sham-operated group; $^{\#}P < 0.05$ compared to the vehicle-treated group. Statistical significance was determined by multifactorial ANOVA. All data are reported as the mean ± s.d.

the phosphorylation of both Smad2/3 and Smad1/5/8 at low concentrations, but the highest amount of pSmad1/5/8 was achieved with a higher dose of TGF-β1 (5 ng ml^{-1}) (**Fig. 4e**). Immunostaining of the subchondral bone showed that the number of pSmad1$^+$ cells remained relatively stable in ACLT mice treated with the TβRI inhibitor relative to sham-operated controls (**Fig. 4f**). In contrast, the number of pSmad2/3$^+$ cells was higher in ACLT mice, and this effect was prevented by TβRI inhibitor treatment (**Fig. 4f**), suggesting that phosphorylation of Smad2/3 is the primary downstream signal of TGF-β in subchondral bone MSCs. Consistently, the expression of ALK1 remained unchanged in ACLT mice treated with vehicle or inhibitor relative to sham-operated control mice, whereas the expression of ALK5 was significantly higher in ACLT mice relative to sham-operated control mice, and this effect was inhibited by injection of

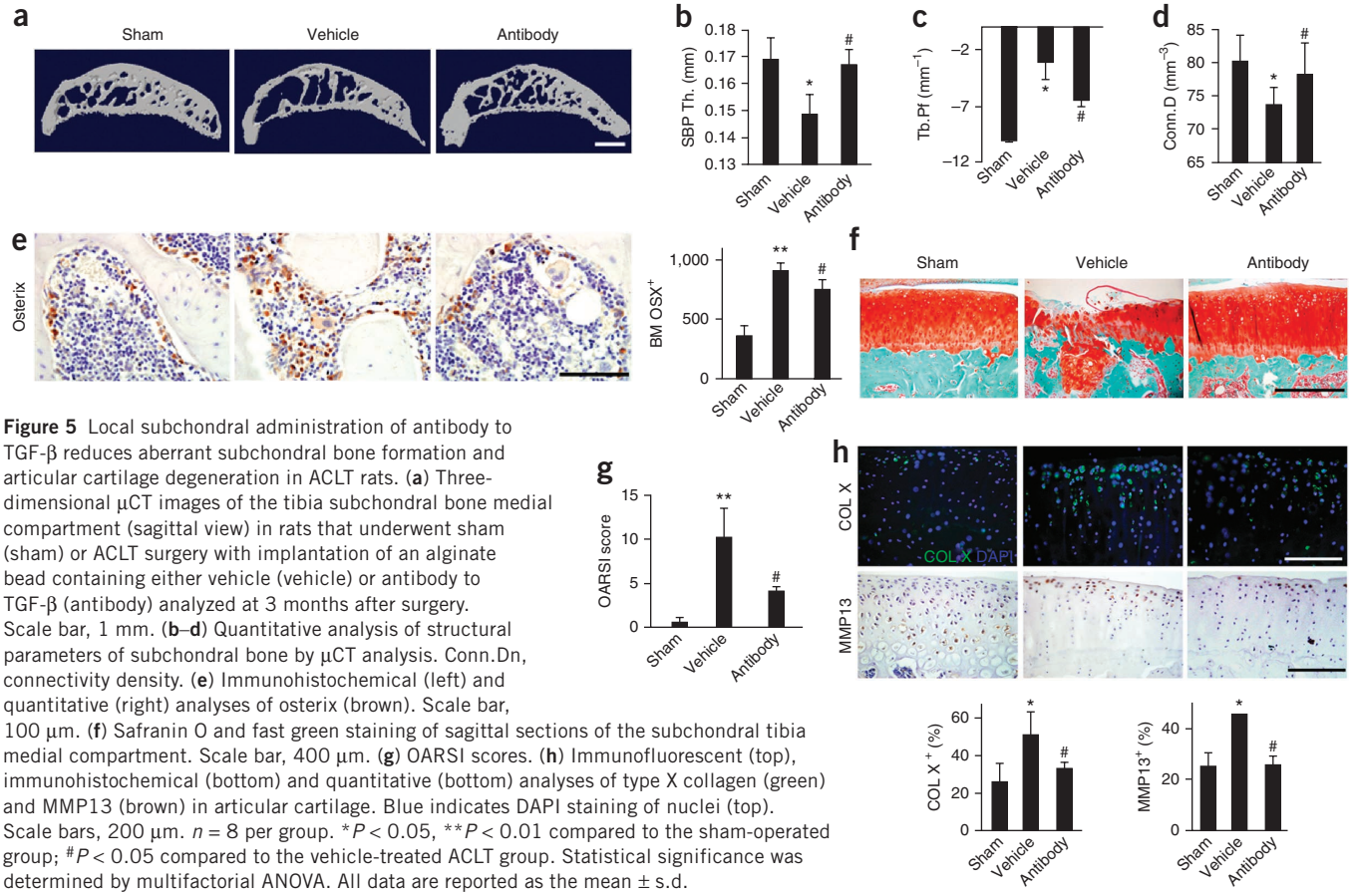

Figure 5 Local subchondral administration of antibody to TGF-β reduces aberrant subchondral bone formation and articular cartilage degeneration in ACLT rats. (**a**) Three-dimensional μCT images of the tibia subchondral bone medial compartment (sagittal view) in rats that underwent sham (sham) or ACLT surgery with implantation of an alginate bead containing either vehicle (vehicle) or antibody to TGF-β (antibody) analyzed at 3 months after surgery. Scale bar, 1 mm. (**b**–**d**) Quantitative analysis of structural parameters of subchondral bone by μCT analysis. Conn.Dn, connectivity density. (**e**) Immunohistochemical (left) and quantitative (right) analyses of osterix (brown). Scale bar, 100 μm. (**f**) Safranin O and fast green staining of sagittal sections of the subchondral tibia medial compartment. Scale bar, 400 μm. (**g**) OARSI scores. (**h**) Immunofluorescent (top), immunohistochemical (bottom) and quantitative (bottom) analyses of type X collagen (green) and MMP13 (brown) in articular cartilage. Blue indicates DAPI staining of nuclei (top). Scale bars, 200 μm. $n = 8$ per group. $^{*}P < 0.05$, $^{**}P < 0.01$ compared to the sham-operated group; $^{\#}P < 0.05$ compared to the vehicle-treated ACLT group. Statistical significance was determined by multifactorial ANOVA. All data are reported as the mean ± s.d.

the TβRI inhibitor (**Fig. 4f**). The number of CD31^{+} endothelial progenitors was significantly higher in the subchondral bone of ACLT mice relative to sham-operated controls, and this effect was reduced by injection of the TβRI inhibitor (**Fig. 4g**).

Microfil contrast–enhanced angiography of subchondral bone confirmed that the inhibitor-treated group had less angiogenesis than the vehicle-treated group (**Fig. 4h**). The contrast signal was substantially stronger in vehicle-treated mice at 1 month after ACLT as compared to vehicle-treated sham-operated mice in magnetic resonance imaging (MRI) perfusion analysis, and we did not detect this stronger signal in the inhibitor-treated group, indicating less new vessel formation (**Fig. 4i** and **Supplementary Fig. 7**). The bone marrow lesion in the tibial subchondral bone detected by micro-MRI was also smaller in the ACLT inhibitor-treated mice compared to in the ACLT vehicle-treated mice (**Fig. 4j**), suggesting the association of bone marrow lesions with osteoid islets. These results indicate that high concentrations of active TGF-β increased the number of nestin-positive MSCs, leading to subchondral bone marrow osteoid islets and angiogenesis, which are pathological changes of this region after ACLT.

Antibody and genetic targeting of TGF-β in osteoarthritis

To validate the role of TGF-β in subchondral bone at the onset of osteoarthritis, we implanted an antibody to TGF-β (1D11)[38,39] in alginate beads[40,41] directly in the tibial subchondral bone of the joints of ACLT rats. We then harvested the knee joints at 3 months after surgery. Similarly to systemic use of the TβRI inhibitor, the microarchitecture of the bone was improved with local application of the antibody as compared to treatment with vehicle in ACLT rats (**Fig. 5a–d**). The number of osterix-positive progenitor clusters in the bone marrow cavities of the joints of ACLT rats was significantly less in the antibody-treated rats compared to in the vehicle-treated rats (**Fig. 5e**).

Notably, degeneration of articular cartilage was attenuated by administration of the antibody in subchondral bone, as reflected in OARSI scores (**Fig. 5f,g**). Moreover, the percentages of MMP13^{+} and type X collagen–positive chondrocytes were lower in the antibody-treated than the vehicle-treated ACLT rats, indicating protection from degeneration of articular cartilage (**Fig. 5h**). In contrast, the elevated MMP13 and type X collagen expression was not abolished by systemic injection of TβRI inhibitor (**Fig. 3g,h**), as TGF-β is essential for the homeostasis of articular cartilage. Therefore, specific administration of the antibody to TGF-β in subchondral bone suppressed aberrant bone formation but did not inhibit TGF-β signaling in articular cartilage. The protective effect on articular cartilage in our rat osteoarthritis model was primarily through an improvement of subchondral bone by site-specific administration of the antibody to TGF-β. These results further validate that the role of TGF-β in the subchondral bone is distinct from its role in articular cartilage; high concentrations of active TGF-β1 in the subchondral bone induced abnormal bone formation, leading to the development of osteoarthritis.

TGF-β binds to a complex of TβRII and TβRI to induce phosphorylation of downstream Smad2/3. Deletion of *Tgfbr2* ensures blocking of the TGF-β signaling cascade. We induced knockout of *Tgfbr2* in nestin-positive MSCs of ACLT mice to confirm the crucial role of TGF-β signaling in MSCs at the onset of osteoarthritis. We injected *Nestin-cre*^{tm}*Er*::*Tgfbr2*$^{flox/flox}$ mice with tamoxifen to delete *Tgfbr2* (*Tgfbr2*$^{-/-}$) in the nestin-positive MSCs that are unresponsive

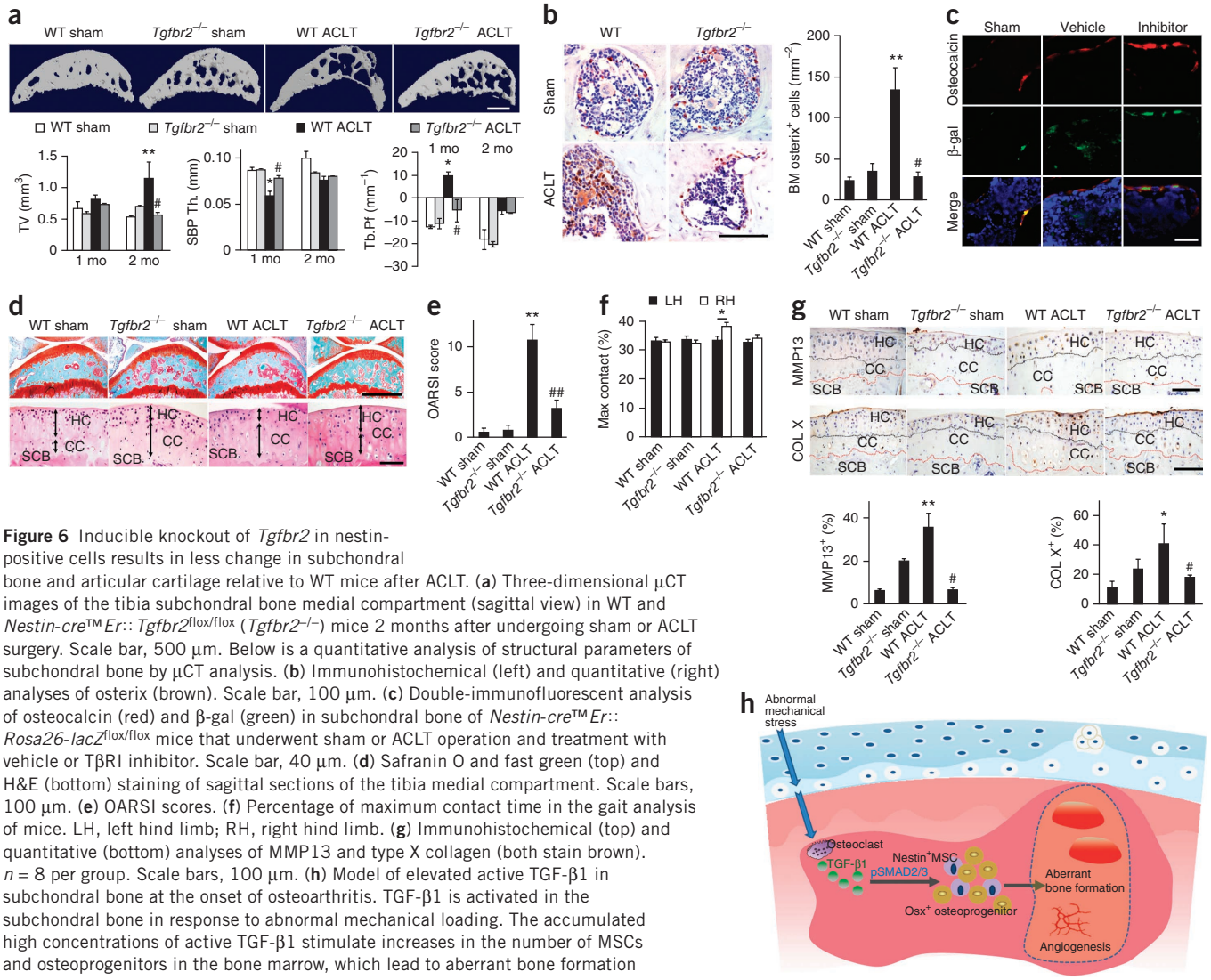

Figure 6 Inducible knockout of *Tgfbr2* in nestin-positive cells results in less change in subchondral bone and articular cartilage relative to WT mice after ACLT. (**a**) Three-dimensional μCT images of the tibia subchondral bone medial compartment (sagittal view) in WT and *Nestin-cre*™*Er*::*Tgfbr2*$^{flox/flox}$ (*Tgfbr2*$^{-/-}$) mice 2 months after undergoing sham or ACLT surgery. Scale bar, 500 μm. Below is a quantitative analysis of structural parameters of subchondral bone by μCT analysis. (**b**) Immunohistochemical (left) and quantitative (right) analyses of osterix (brown). Scale bar, 100 μm. (**c**) Double-immunofluorescent analysis of osteocalcin (red) and β-gal (green) in subchondral bone of *Nestin-cre*™*Er*::*Rosa26-lacZ*$^{flox/flox}$ mice that underwent sham or ACLT operation and treatment with vehicle or TβRI inhibitor. Scale bar, 40 μm. (**d**) Safranin O and fast green (top) and H&E (bottom) staining of sagittal sections of the tibia medial compartment. Scale bars, 100 μm. (**e**) OARSI scores. (**f**) Percentage of maximum contact time in the gait analysis of mice. LH, left hind limb; RH, right hind limb. (**g**) Immunohistochemical (top) and quantitative (bottom) analyses of MMP13 and type X collagen (both stain brown). $n = 8$ per group. Scale bars, 100 μm. (**h**) Model of elevated active TGF-β1 in subchondral bone at the onset of osteoarthritis. TGF-β1 is activated in the subchondral bone in response to abnormal mechanical loading. The accumulated high concentrations of active TGF-β1 stimulate increases in the number of MSCs and osteoprogenitors in the bone marrow, which lead to aberrant bone formation and angiogenesis for osteoarthritis progression. $^{*}P < 0.05$, $^{**}P < 0.01$ compared to the WT sham-operated group; $^{\#}P < 0.05$, $^{\#\#}P < 0.01$ compared to the WT ACLT group. Statistical significance was determined by multifactor ANOVA, except for in **f**, in which paired *t* test was used. All data are reported as the mean ± s.d.

to TGF-β, whereas the TGF-β signaling pathway in other cell types, including chondrocytes, remained intact (**Supplementary Fig. 8**). Similarly to with TβRI inhibitor treatment, the microarchitecture and Tb.Pf were significantly improved in the ACLT *Tgfbr2*$^{-/-}$ mice at 2 months after surgery relative to the ACLT WT littermates (**Fig. 6a**). Osterix-positive osteoprogenitors in the subchondral bone remained primarily on the bone surface, similarly to in ACLT WT littermates (**Fig. 6b**). Moreover, co-staining of β-galactosidase (β-gal) and osteocalcin in the subchondral bone of *Nestin-cre*™*Er*::*Rosa26-lacZ*$^{flox/flox}$ mice revealed that the β-gal^{+} MSC lineage cells were located in the bone marrow in the vehicle-treated ACLT mice, whereas β-gal^{+} cells were distributed primarily on the bone surface and were osteocalcin positive in sham-operated controls and TβRI inhibitor–treated ACLT mice (**Fig. 6c**). There was less proteoglycan loss in articular cartilage in the *Tgfbr2*$^{-/-}$ mice as compared to in the WT mice after ACLT (**Fig. 6d**). Calcification of articular cartilage was also attenuated, and the thickness of the calcified cartilage remained unchanged relative to ACLT WT mice (**Fig. 6d**). Immunostaining demonstrated that the expression of MMP13 and type X collagen was significantly inhibited in ACLT *Tgfbr2*$^{-/-}$ mice relative to ACLT WT littermates, indicating inhibition of articular cartilage degeneration (**Fig. 6**). The protective effects on articular cartilage in ACLT *Tgfbr2*$^{-/-}$ mice were reflected in OARSI scores (**Fig. 6e**). The disparity between the percentage of maximum contact time of the two hind limbs in WT ACLT mice did not occur in ACLT *Tgfbr2*$^{-/-}$ littermates, as revealed by gait analysis (**Fig. 6f**). Thus, these data further demonstrate that high concentrations of TGF-β initiate pathological changes in subchondral bone MSCs, contributing to the onset of osteoarthritis.

DISCUSSION

TGF-β is known for its anabolic effects on articular cartilage homeostasis by stimulating the production of extracellular matrix proteins and preventing terminal differentiation of chondrocytes[42,43]. In this study we found that changes in mechanical loading on joints were associated with a higher number of osteoclasts in the subchondral bone as early as 7 d after surgery in the ACLT mouse model. High concentrations of TGF-β1 were activated during osteoclast bone resorption to recruit nestin-positive MSCs for the subsequent uncoupled bone formation.

Notably, osteoclastic bone resorption was spatiotemporally uncoupled with TGF-β1–induced recruitment of nestin-positive MSCs and led to aberrant bone formation, which was further substantiated by the development of osteoarthritic-like changes in CED mice.

Relative to a single phase of uncoupled sequential bone resorption and formation in the mouse ACLT model, human osteoarthritis was more complex and had multiple phases. We found that some areas of the articular cartilage were still intact or were in the middle stage of osteoarthritis progression when analyzing specimens from subjects with late-stage osteoarthritis who underwent knee joint replacement. Consistently, the thickness of the SBP in specimens from individuals with osteoarthritis was not uniform, although the percentage distribution of the SBP was generally thicker compared to healthy subjects. Moreover, the concentrations of active TGF-β were higher in subchondral bone with articular cartilage compared to bone from healthy controls. This observation suggests that inhibition of TGF-β activity in the subchondral bone may have therapeutic effects even if individuals with osteoarthritis are not in the early stages. Our findings also reveal that TGF-β has a different role in subchondral bone as compared to its anabolic effect on articular cartilage. Thus, the location of the elevated TGF-β1 concentrations in subchondral bone triggers a cascade of events that lead to the development of osteoarthritis.

Clinical studies have reported that progression of osteoarthritis is accompanied by the accumulation of mesenchymal progenitor cells in joint tissues and synovial fluids[44,45]. Bone marrow lesions have been identified as a prognostic factor of osteoarthritis progression, as they have been found to populate sites of cartilage destruction[16,17,46]. We found that elevations in TGF-β1 concentrations lead to a high number of nestin-positive MSCs in the subchondral bone marrow in various osteoarthritis rodent models. During the normal remodeling process, osteoblasts and their progenitors are located primarily at the resorption site on the bone surface. However, the altered microenvironment induced by abnormal mechanical loading may lead to *in situ* commitment of osteoprogenitors in bone marrow cavities. Bone marrow lesions have been characterized as less well–mineralized newly formed bone[46]. These clustered bone marrow osteoprogenitors may lead to osteoid islets in the subchondral bone marrow that are visualized as bone marrow lesions during MRI. Moreover, knockout of *Tgfbr2* in nestin-positive MSCs attenuated the development of osteoarthritis in ACLT mice. This result further confirmed our hypothesis that MSCs are the target cells of aberrant TGF-β signals during osteoarthritis progression. Additionally, bone formation is often coupled with angiogenesis. It is known that the TGF-β signaling pathway in endothelial progenitor cells can promote angiogenesis[47], and TGF-β may stimulate the paracrine machinery in MSCs that further facilitates angiogenesis[48,49]. Our data revealed that the numbers of blood vessels were high in the subchondral bone of both ACLT and CED mice, as determined by angiography in microphil-perfused experiments. Low angiogenesis caused by inhibition of TGF-β activity may have further attenuated the *de novo* bone formation in the subchondral bone in the osteoarthritis joints of ACLT mice.

The subchondral bone and articular cartilage act as a functional unit in the joint[10]. In human osteoarthritis joints, the SBPs are markedly thicker relative to those of healthy subjects[50]. We modeled the subchondral bone after surgery in ACLT rodent models and found that its thickness fluctuated substantially. The capacity of chondrocytes to modulate their functional state in response to alterations in mechanical loading is relatively limited compared to in the adjacent subchondral bone. Changes in osteochondral junction are therefore probably involved in advancement of the calcified cartilage zone[51–53]. The formation of osteoid islets in the subchondral bone marrow probably precedes degeneration of articular cartilage. The results of our study suggest that careful titration of TGF-β activity inhibition may be a possible avenue for the prevention of osteoarthritis or the treatment of its early stages.

METHODS

Methods and any associated references are available in the online version of the paper.

Note: Supplementary information is available in the online version of the paper.

ACKNOWLEDGMENTS

This research was supported by US National Institutes of Health grants DK 057501 and DK 08098 (both to X.C.). We thank R. Luck and L. Sakowski for collecting samples.

AUTHOR CONTRIBUTIONS

G.Z. conceived the ideas for experimental designs, conducted the majority of the experiments, analyzed data and prepared the manuscript. C.W. conducted some of the surgery, performed MRI and μCT analyses and helped with manuscript preparation. X.J. provide ideas and helped with behavior analysis. Y.L. conduced cell culture, western blot and behavior analysis and helped with manuscript preparation. J.L.C., W.C. and M.W. helped compose the manuscript. S.C.M., F.B.A., F.J.F., A.C. and P.S. provided human specimens. D.A. and J.A.C. helped with MRI analysis. J.Y. performed computerized simulation. Q.C., X.Z., L.R., Z.Z. and W.W.L. provided suggestions for the project. X.C. developed the concept, supervised the project, conceived the experiments and wrote most of the manuscript.

COMPETING FINANCIAL INTERESTS

The authors declare no competing financial interests.

1. Hootman, J.M. & Helmick, C.G. Projections of US prevalence of arthritis and associated activity limitations. *Arthritis Rheum.* **54**, 226–229 (2006).
2. van den Berg, W.B. Osteoarthritis year 2010 in review: pathomechanisms. *Osteoarthritis Cartilage* **19**, 338–341 (2011).
3. Berenbaum, F. Osteoarthritis year 2010 in review: pharmacological therapies. *Osteoarthritis Cartilage* **19**, 361–365 (2011).
4. Hawker, G.A., Mian, S., Bednis, K. & Stanaitis, I. Osteoarthritis year 2010 in review: non-pharmacologic therapy. *Osteoarthritis Cartilage* **19**, 366–374 (2011).
5. Saito, T. *et al.* Transcriptional regulation of endochondral ossification by HIF-2α during skeletal growth and osteoarthritis development. *Nat. Med.* **16**, 678–686 (2010).
6. Yang, S. *et al.* Hypoxia-inducible factor-2α is a catabolic regulator of osteoarthritic cartilage destruction. *Nat. Med.* **16**, 687–693 (2010).
7. Wang, Q. *et al.* Identification of a central role for complement in osteoarthritis. *Nat. Med.* **17**, 1674–1679 (2011).
8. Glasson, S.S. *et al.* Deletion of active ADAMTS5 prevents cartilage degradation in a murine model of osteoarthritis. *Nature* **434**, 644–648 (2005).
9. Neuhold, L.A. *et al.* Postnatal expression in hyaline cartilage of constitutively active human collagenase-3 (MMP-13) induces osteoarthritis in mice. *J. Clin. Invest.* **107**, 35–44 (2001).
10. Lories, R.J. & Luyten, F.P. The bone-cartilage unit in osteoarthritis. *Nat. Rev. Rheumatol.* **7**, 43–49 (2011).
11. Madry, H., van Dijk, C.N. & Mueller-Gerbl, M. The basic science of the subchondral bone. *Knee Surg. Sports Traumatol. Arthrosc.* **18**, 419–433 (2010).
12. Burr, D.B. & Radin, E.L. Microfractures and microcracks in subchondral bone: are they relevant to osteoarthrosis? *Rheum. Dis. Clin. North Am.* **29**, 675–685 (2003).
13. Stein, V. *et al.* Pattern of joint damage in persons with knee osteoarthritis and concomitant ACL tears. *Rheumatol. Int.* **32**, 1197–1208 (2012).
14. Amin, S. *et al.* Complete anterior cruciate ligament tear and the risk for cartilage loss and progression of symptoms in men and women with knee osteoarthritis. *Osteoarthritis Cartilage* **16**, 897–902 (2008).
15. Hill, C.L. *et al.* Cruciate ligament integrity in osteoarthritis of the knee. *Arthritis Rheum.* **52**, 794–799 (2005).
16. Suri, S. & Walsh, D.A. Osteochondral alterations in osteoarthritis. *Bone* **51**, 204–211 (2012).
17. Hunter, D.J. *et al.* Increase in bone marrow lesions associated with cartilage loss: a longitudinal magnetic resonance imaging study of knee osteoarthritis. *Arthritis Rheum.* **54**, 1529–1535 (2006).

18. Dreier, R. Hypertrophic differentiation of chondrocytes in osteoarthritis: the developmental aspect of degenerative joint disorders. *Arthritis Res. Ther.* **12**, 216 (2010).
19. Tchetina, E.V. Developmental mechanisms in articular cartilage degradation in osteoarthritis. *Arthritis* **2011**, 683970 (2011).
20. Blaney Davidson, E.N., van der Kraan, P.M. & van den Berg, W.B. TGF-β and osteoarthritis. *Osteoarthritis Cartilage* **15**, 597–604 (2007).
21. Yang, X. *et al.* TGF-β/Smad3 signals repress chondrocyte hypertrophic differentiation and are required for maintaining articular cartilage. *J. Cell Biol.* **153**, 35–46 (2001).
22. Wu, Q. *et al.* Induction of an osteoarthritis-like phenotype and degradation of phosphorylated Smad3 by Smurf2 in transgenic mice. *Arthritis Rheum.* **58**, 3132–3144 (2008).
23. Blaney Davidson, E.N. *et al.* Increase in ALK1/ALK5 ratio as a cause for elevated MMP-13 expression in osteoarthritis in humans and mice. *J. Immunol.* **182**, 7937–7945 (2009).
24. van der Kraan, P.M., Blaney Davidson, E.N., Blom, A. & van den Berg, W.B. TGF-β signaling in chondrocyte terminal differentiation and osteoarthritis: modulation and integration of signaling pathways through receptor-Smads. *Osteoarthritis Cartilage* **17**, 1539–1545 (2009).
25. van der Kraan, P.M., Blaney Davidson, E.N. & van den Berg, W.B. A role for age-related changes in TGFβ signaling in aberrant chondrocyte differentiation and osteoarthritis. *Arthritis Res. Ther.* **12**, 201 (2010).
26. Scharstuhl, A. *et al.* Inhibition of endogenous TGF-β during experimental osteoarthritis prevents osteophyte formation and impairs cartilage repair. *J. Immunol.* **169**, 507–514 (2002).
27. Scharstuhl, A., Vitters, E.L., van der Kraan, P.M. & van den Berg, W.B. Reduction of osteophyte formation and synovial thickening by adenoviral overexpression of transforming growth factor β/bone morphogenetic protein inhibitors during experimental osteoarthritis. *Arthritis Rheum.* **48**, 3442–3451 (2003).
28. Tang, Y. *et al.* TGF-β1–induced migration of bone mesenchymal stem cells couples bone resorption with formation. *Nat. Med.* **15**, 757–765 (2009).
29. Hahn, M., Vogel, M., Pompesius-Kempa, M. & Delling, G. Trabecular bone pattern factor—a new parameter for simple quantification of bone microarchitecture. *Bone* **13**, 327–330 (1992).
30. Pritzker, K.P. *et al.* Osteoarthritis cartilage histopathology: grading and staging. *Osteoarthritis Cartilage* **14**, 13–29 (2006).
31. Shi, M. *et al.* Latent TGF-β structure and activation. *Nature* **474**, 343–349 (2011).
32. Whyte, M.P. *et al.* Camurati-Engelmann disease: unique variant featuring a novel mutation in TGFβ1 encoding transforming growth factor β 1 and a missense change in TNFSF11 encoding RANK ligand. *J. Bone Miner. Res.* **26**, 920–933 (2011).
33. Lotz, M. Osteoarthritis year 2011 in review: biology. *Osteoarthritis Cartilage* **20**, 192–196 (2012).
34. Méndez-Ferrer, S. *et al.* Mesenchymal and haematopoietic stem cells form a unique bone marrow niche. *Nature* **466**, 829–834 (2010).
35. Wiese, C. *et al.* Nestin expression—a property of multi-lineage progenitor cells? *Cell Mol. Life Sci.* **61**, 2510–2522 (2004).
36. Kamekura, S. *et al.* Osteoarthritis development in novel experimental mouse models induced by knee joint instability. *Osteoarthritis Cartilage* **13**, 632–641 (2005).
37. Goumans, M.J. *et al.* Balancing the activation state of the endothelium via two distinct TGF-β type I receptors. *EMBO J.* **21**, 1743–1753 (2002).
38. Lorts, A., Schwanekamp, J.A., Baudino, T.A., McNally, E.M. & Molkentin, J.D. Deletion of periostin reduces muscular dystrophy and fibrosis in mice by modulating the transforming growth factor-β pathway. *Proc. Natl. Acad. Sci. USA* **109**, 10978–10983 (2012).
39. Edwards, J.R. *et al.* Inhibition of TGF-β signaling by 1D11 antibody treatment increases bone mass and quality *in vivo*. *J. Bone Miner. Res.* **25**, 2419–2426 (2010).
40. Ma, Y., Li, W.Z., Guan, S.X., Lai, X.P. & Chen, D.W. Evaluation of tetrandrine sustained release calcium alginate gel beads *in vitro* and *in vivo*. *Yakugaku Zasshi* **129**, 851–854 (2009).
41. Downs, E.C., Robertson, N.E., Riss, T.L. & Plunkett, M.L. Calcium alginate beads as a slow-release system for delivering angiogenic molecules *in vivo* and *in vitro*. *J. Cell Physiol.* **152**, 422–429 (1992).
42. Zhang, M. *et al.* Smad3 prevents β-catenin degradation and facilitates β-catenin nuclear translocation in chondrocytes. *J. Biol. Chem.* **285**, 8703–8710 (2010).
43. Li, T.F. *et al.* Smad3-deficient chondrocytes have enhanced BMP signaling and accelerated differentiation. *J. Bone Miner. Res.* **21**, 4–16 (2006).
44. Sekiya, I. *et al.* Human mesenchymal stem cells in synovial fluid increase in the knee with degenerated cartilage and osteoarthritis. *J. Orthop. Res.* **30**, 943–949 (2012).
45. Koyama, N. *et al.* Pluripotency of mesenchymal cells derived from synovial fluid in patients with temporomandibular joint disorder. *Life Sci.* **89**, 741–747 (2011).
46. Hunter, D.J. *et al.* Bone marrow lesions from osteoarthritis knees are characterized by sclerotic bone that is less well mineralized. *Arthritis Res. Ther.* **11**, R11 (2009).
47. Cunha, S.I. & Pietras, K. ALK1 as an emerging target for antiangiogenic therapy of cancer. *Blood* **117**, 6999–7006 (2011).
48. Guiducci, S. *et al.* Bone marrow–derived mesenchymal stem cells from early diffuse systemic sclerosis exhibit a paracrine machinery and stimulate angiogenesis *in vitro*. *Ann. Rheum. Dis.* **70**, 2011–2021 (2011).
49. Kasper, G. *et al.* Mesenchymal stem cells regulate angiogenesis according to their mechanical environment. *Stem Cells* **25**, 903–910 (2007).
50. Li, B. & Aspden, R.M. Mechanical and material properties of the subchondral bone plate from the femoral head of patients with osteoarthritis or osteoporosis. *Ann. Rheum. Dis.* **56**, 247–254 (1997).
51. Goldring, S.R. Alterations in periarticular bone and cross talk between subchondral bone and articular cartilage in osteoarthritis. *Ther. Adv. Musculoskelet. Dis.* **4**, 249–258 (2012).
52. Goldring, S.R. Role of bone in osteoarthritis pathogenesis. *Med. Clin. North Am.* **93**, 25–35 (2009).
53. Goldring, M.B. & Goldring, S.R. Osteoarthritis. *J. Cell. Physiol.* **213**, 626–634 (2007).

ONLINE METHODS

Human subjects. After approval by the Institutional Review Board of Johns Hopkins University, we collected tibial plateau specimens from 78 individuals with osteoarthritis that were undergoing total knee replacement surgery. The specimens were processed for μCT, ELISA and histological examination. We purchased healthy knee specimens from the Nation Disease Research Interchange (NDRI) to serve as controls.

Mice. We purchased C57BL/6J (WT) mice from Charles River. We anesthetized male mice from this group at 2 months of age with ketamine and xylazine and then transected the ACL surgically to induce mechanical instability–associated osteoarthritis on the left knee. Sham operations were done on independent mice. For the time-course experiments, operated mice were euthanized at 0, 7, 14, 30, 60 or 90 d after surgery ($n = 8$–12 per group). For the dosage screening experiments, 2-month-old sham-operated and ACLT mice were assigned into six groups, with ten mice per group. Beginning 3 d after surgery, we injected either different doses (0.1, 0.5, 1, 2.5 or 5 mg per kg body weight) of TβRI inhibitor (SB-505124, Sigma-Aldrich) or the equivalent volume of vehicle (DMSO and PBS) intraperitoneally daily for 30 d. Mice were euthanized 30 or 60 d after surgery.

We purchased *Nestin-cre™Er* and *(ROSA)26Sortm1Sor/J* mice from the Jackson Laboratory. Mice with floxed *Tgfbr2* (*Tgfbr2*$^{flox/flox}$) were obtained from the lab of H.L. Moses[54]. *Nestin-cre™Er* mice were crossed with *Tgfbr2*$^{flox/flox}$ mice. The offspring were intercrossed to generate *Nestin-cre™Er*::*Tgfbr2*$^{flox/flox}$ offspring, in which *cre* was fused with a mutated gene of estrogen receptor (Er). Er could be activated by tamoxifen (TM). We determined the genotype of the transgenic mice by PCR analyses of genomic DNA isolated from mouse tails. Genotyping for the Cre transgene was performed by PCR with the primers for *cre* 5′-CAAATAGCCCTGGCA GAT-3′ and 5′-TGATACAAGGGACATCTTCC-3′. The *loxP Tgfbr2* allele was identified with the primers forward, 5′-TAAACAAGGTCCGGAGCCCA-3′ and reverse, 5′-ACTTCTGCAAGAGGTCCCCT-3′ (ref. 55). We generated *Nestin-cre™Er*::*Rosa26-lacZ* $^{flox/flox}$ mice by crossing *Nestin-cre™Er* mice with mice homozygous with a *loxP*-flanked DNA stop sequence, preventing expression of the downstream *lacZ* gene. The offspring were then intercrossed to generate the following genotype: *Nestin-cre™Er*::*Rosa26-lacZ*$^{flox/flox}$. We performed sham or ACLT operations on 2-month-old male WT, *Nestin-cre™Er*::*Tgfbr2*$^{flox/flox}$ and *Nestin-cre™Er*::*Rosa26-lacZ*$^{flox/flox}$ mice. Three days after surgery, we treated each group with 100 mg per kg body weight of tamoxifen daily for 30 d and euthanized the mice at either 30 or 60 d after surgery ($n = 8$ per treatment group). CED mice were generated in our laboratory as previously described, in which the CED-derived TGF-β1 mutation (H222D) is specifically expressed by osteoblastic cells driven by a 2.3-kb type I collagen promoter[28].

Rats. We purchased 2-month-old male Lewis rats from Charles River. ACLT was conducted as described as above. After ACLT, we made a canal in the medial plateau using a 20G needle. An alginate bead containing 0.1 μg 1D11 (TGF-β1–neutralizing antibody; R&D Systems, Minneapolis, MN) or vehicle was embedded in the subchondral bone canal. The canal was then closed with bone wax. We euthanized the rats at 0, 1, 2 or 3 months after surgery ($n = 8$ per group). Knee joints were processed for μCT and histological analysis.

All animals (rat and mouse) were maintained in the Animal Facility of the Johns Hopkins University School of Medicine. The experimental protocols for both species were reviewed and approved by the Institutional Animal Care and Use Committee of the Johns Hopkins University, Baltimore, MD, USA.

Cell culture. We obtained GFP-labeled mouse adult MSCs from the Texas A&M Health Science Center College of Medicine Institute (College Station). We maintained cells (passage 3–5) in Iscove's modified Dulbecco's medium (Invitrogen) supplemented with 10% FCS (Atlanta Biologicals), 10% horse serum (Thermo Scientific) and 1% penicillin-streptomycin (Mediatech). We cultured MSCs in six-well plates at a density of 1.8×10^5 cells per well, starved them for 6 h and then treated them with TGF-β1 (R&D Systems) or TβRI inhibitor (SB-505124) (Sigma-Aldrich), as indicated.

ELISA and western blot. We determined the concentration of active TGF-β1 in the conditioned medium using the ELISA Development kit (R&D Systems) according to the manufacturer's instructions. Western blot analyses were conducted on the protein of lysates from *in vitro*–cultured MSCs. The cell lysates were centrifuged, and the supernatants were separated by SDS-PAGE and blotted on a polyvinylidene fluoride membrane (Bio-Rad Laboratories). After incubation in specific antibodies, we detected proteins using an enhanced chemiluminescence kit (Amersham Biosciences). We used antibodies recognizing mouse pSmad1/5 (Cell Signaling Technology Inc., 1:500, 9516), pSmad2 (Cell Signaling Technology Inc., 1:1,000, 3108), Smad1 (Cell Signaling Technology Inc., 1:1,000, 9743) and Smad2 (Cell Signaling Technology Inc., 1:1,000, 3103) to examine the protein concentrations in the lysates.

Histochemistry, immunohistochemistry and histomorphometry. At the time of euthanasia, we resected and fixed the knee joints in 10% buffered formalin for 48 h, decalcified them in 10% EDTA (pH 7.4) for 14 d and embedded them in paraffin or optimal cutting temperature (OCT) compound (Sakura Finetek). Four-micrometer-thick sagittal-oriented sections of the knee joint medial compartment were processed for H&E and safranin O and fast green staining. Tartrate-resistant acid phosphatase staining was performed using a standard protocol (Sigma-Aldrich). Immunostaining was performed using a standard protocol. We incubated sections with primary antibodies to mouse nestin (Aves Labs, Inc., 1:300, lot NES0407), osterix (Abcam, 1:600, ab22552), osteocalcin (Takara Bio Inc., 1:200, M137), pSmad2/3 (Santa Cruz Biotechnology Inc., 1:50, sc-11769), pSmad1 (Abcam, 1:50, ab63439), ALK1 (Santa Cruz Biotechnology Inc., 1:50, sc-28976), ALK5 (Abcam, 1:50, ab31013), CD31 (Abcam, 1:100, ab28364), MMP13 (Abcam, 1:40, ab3208) and collagen X (Abcam, 1:80, ab58632) overnight at 4 °C. For immunohistochemical staining, a horse radish peroxidase–streptavidin detection system (Dako) was subsequently used to detect the immunoactivity, followed by counterstaining with hematoxylin (Sigma-Aldrich). For immunofluorescent staining, secondary antibodies conjugated with fluorescence were added, and slides were incubated at room temperature for 1 h while avoiding light. We microphotographed sections to perform histomorphometric measurements on the entire area of the tibia subchondral bone (Olympus DP71). Quantitative histomorphometric analysis was conducted in a blinded fashion with OsteoMeasureXP Software (OsteoMetrics, Inc.). To label mineralization deposition, sequential subcutaneous injections of 1% calcein (Sigma; 15 mg per kg body weight) and 3% xylenol orange (Sigma; 90 mg per kg body weight) in 2% sodium bicarbonate solution were performed. Calcein and xylenol orange were injected 10 d and 2 d, respectively, before the mice were euthanized. We counted the number of positively stained cells in the whole tibia subchondral bone area per specimen in five sequential sections per mouse in each group. We calculated OARSI scores as previously described[30].

Flow cytometry. We divided C57BL/6J mice into three groups ($n = 10$ per group): sham operation with vehicle treatment, ACLT with vehicle treatment, and ACLT with TβRI inhibitor (SB-505124) treatment. One month after surgery, we euthanized the mice and pooled the tibia subchondral bone marrow cells from each group together. Red blood cells were lysed by commercial ACK lysis buffer (Quality Biological, Inc.). After centrifugation (1,200 r.p.m., 5 min at room temperature), the cell pellet was resuspended and fixed in 4% paraformaldehyde. We then washed cells with 0.1% BSA in PBS and counted them. One million cells per milliliter were permeabilized in 0.1% Triton X-100 before blocking in 3% FACS buffer (PBS, 3% FBS and 0.1% NaN_3 sodium azide) for 30 min on ice. We incubated the cells with Alexa Fluor 647–conjugated antibody to nestin (BD Pharmingen, 1:100, 560393), antibody to osterix (Abcam, 1:400, ab22552) or isotype control antibody for 1 h at 37 °C in a dark room and then washed them twice with 0.1% BSA in PBS. The cells for osterix staining were further incubated with fluorescein isothiocyanate (FITC)-conjugated secondary antibody (Abcam, 1:500, ab6798) for 30 min on ice. The cells were acquired immediately after washing with 3% FACS buffer. Probes were analyzed using a FACS Calibur flow cytometer and CellQuest software (Becton Dickinson).

***In vivo* micro-MRI.** We performed all MRI studies on a horizontal 30-cm-bore 9.4T Bruker Biospec preclinical scanner using a custom-built, single-turn volume coil positioned orthogonal to the B_0 magnetic field[56,57]. Anesthesia was initiated with 4% isoflurane and maintained with a 2% isoflurane and oxygen mixture.

We acquired T2-weighted images with a two-dimensional RARE (rapid acquisition with relaxation enhancement) sequence, a TE/TR (echo time/repetition time) of 15.17 ms/3,000 ms, 35 slices at thickness of 0.35 mm, field of view (FOV) of 1.75 cm × 1.75 cm and matrix size of 256 × 128. We acquired T2-weighted images with a chemical shift–selective fat saturation pulse tuned to the fat resonant frequency. All T2-weighted images were processed to a final matrix size of 256 × 256 with an isotropic resolution of 0.068 mm pixel^{-1}. We acquired T1-weighted images with a three-dimensional gradient echo sequence using a 30° flip angle, a TE/TR of 1.5 ms/8 ms, FOV of 1.5 cm × 1.5 cm × 1.5 cm and matrix size of 128 × 64 × 64 before and for 10 min after the injection of 0.1 ml 0.1 M gadopentetate dimeglumine. All T1-weighted images were processed to a final matrix size of 128 × 128 × 128 with an isotropic resolution of 0.12 mm pixel^{-1}.

μCT. We dissected knee joints from mice free of soft tissue, fixed them overnight in 70% ethanol and analyzed them by high-resolution μCT (Skyscan1172)[58]. We reconstructed and analyzed images using NRecon v1.6 and CTAn v1.9, respectively. Three-dimensional model visualization software, CTVol v2.0, was used to analyze parameters of the trabecular bone in the epiphysis. The scanner was set at a voltage of 50 kVp, a current of 200 μA and a resolution of 5.7 μm per pixel. Sagittal images of the tibiae subchondral bone were used to perform three-dimensional histomorphometric analyses. We defined the region of interest to cover the whole subchondral bone medial compartment, and we used a total of five consecutive images from the medial tibial plateau for three-dimensional reconstruction and analysis. Three-dimensional structural parameters analyzed included: TV (total tissue volume; contains both trabecular and cortical bone), BV/TV (trabecular bone volume per tissue volume), Tb.Th (trabecular thickness), Tb.Sp (trabecular separation), SMI (structure model index), Conn.Dn (connectivity density) and Tb.Pf (trabecular pattern factor).

CT-based microangiography. We imaged blood vessels in bone by angiography of microphil-perfused bones[59]. Briefly, after we euthanized the animals and opened the thoracic cavity, the inferior vena cava was severed. We flushed the vascular system with 0.9% normal saline solution containing heparin sodium (100 U ml^{-1}) through a needle inserted into the left ventricle. The specimens were pressure fixed with 10% neutral buffered formalin. We washed formalin from the vessels using heparinized saline solution and then injected a radiopaque silicone rubber compound containing lead chromate (Microfil MV-122, Flow Tech) to label the vasculature. Samples were stored at 4 °C overnight for contrast agent polymerization. Mouse knee joints were dissected from the specimens and soaked for 4 d in 10% neutral buffered formalin to ensure complete tissue fixation. We treated specimens for 48 h in a formic acid–based solution (Cal-Ex II) to decalcify the bone and facilitate image thresholding of the femoral vasculature from the surrounding tissues. Images were obtained using a μCT imaging system (Skyscan 1172) at a resolution of a 9 μm isotropic voxel size. A threshold of 60 was initially chosen on the basis of visual interpretation of threshold two-dimensional tomograms.

Gait analysis. We performed automated gait analysis before surgery and 2, 4, 6 and 8 weeks after surgery using a CatWalk system (Noldus). All experiments were performed during the same period of the day (1 p.m. to 4 p.m.) and analyzed as previously reported[60,61]. Briefly, we trained mice to cross the CatWalk walkway daily for 7 d before ACLT or sham operation. During the test, each mouse was placed individually in the CatWalk walkway, which consists of a glass plate (100 cm × 15 cm × 0.6 cm), plus two Plexiglas walls spaced 8 cm apart. The mouse was allowed to walk freely and traverse from one side to the other of the walkway glass plate. Two infrared light beams spaced 90 cm apart were used to detect the arrival of the mouse and control the start and end of data acquisition. We carried the recordings out when the room was completely dark, with the exception of the light from the computer screen. An LED light from an encased fluorescent lamp was emitted inside the glass plate and completely internally reflected. When the mouse paws made contact with the glass plate, light was reflected down and the illuminated contact area was recorded with a high-speed color video camera positioned underneath the glass plate connected to a computer running Catwalk software v9.1 (Noldus). Comparison was made between the ipsilateral (left) and the contralateral (right) hind paw in each run of each animal at each time point. Paired *t* test was used for statistical analyses.

Statistics. Data are presented as the mean ± s.d. The comparisons for OARSI scores, bone mass and microarchitecture among different groups were performed using multifactorial ANOVA. When ANOVA testing indicated overall significance of main effects without interaction between them, the difference between individual time points and sites was assessed by *post hoc* tests. The level of significance was set at $P < 0.05$. All data analyses were performed using SPSS 15.0 analysis software (SPSS Inc).

54. Chytil, A., Magnuson, M.A., Wright, C.V. & Moses, H.L. Conditional inactivation of the TGF-β type II receptor using Cre:Lox. *Genesis* **32**, 73–75 (2002).
55. Qiu, T. *et al.* TGF-β type II receptor phosphorylates PTH receptor to integrate bone remodelling signalling. *Nat. Cell Biol.* **12**, 224–234 (2010).
56. Jones, M.D. *et al. In vivo* microfocal computed tomography and micro-magnetic resonance imaging evaluation of antiresorptive and antiinflammatory drugs as preventive treatments of osteoarthritis in the rat. *Arthritis Rheum.* **62**, 2726–2735 (2010).
57. Lee, J.H. *et al.* Subchondral fluid dynamics in a model of osteoarthritis: use of dynamic contrast-enhanced magnetic resonance imaging. *Osteoarthritis Cartilage* **17**, 1350–1355 (2009).
58. Wu, X. *et al.* Inhibition of Sca-1–positive skeletal stem cell recruitment by alendronate blunts the anabolic effects of parathyroid hormone on bone remodeling. *Cell Stem Cell* **7**, 571–580 (2010).
59. Cao, X. *et al.* Irradiation induces bone injury by damaging bone marrow microenvironment for stem cells. *Proc. Natl. Acad. Sci. USA* **108**, 1609–1614 (2011).
60. Angeby-Möller, K., Berge, O.G. & Hamers, F.P. Using the CatWalk method to assess weight-bearing and pain behaviour in walking rats with ankle joint monoarthritis induced by carrageenan: effects of morphine and rofecoxib. *J. Neurosci. Methods* **174**, 1–9 (2008).
61. Hamers, F.P., Koopmans, G.C. & Joosten, E.A. CatWalk-assisted gait analysis in the assessment of spinal cord injury. *J. Neurotrauma* **23**, 537–548 (2006).

doi:10.1038/nm.3143